6-16-2021

Functional Role of the N-terminal Domain in Connexin 46/50 by *in silico* Mutagenesis and Molecular Dynamics Simulation

Umair Khan
Portland State University

Recommended Citation

Khan, Umair, "Functional Role of the N-terminal Domain in Connexin 46/50 by *in silico* Mutagenesis and Molecular Dynamics Simulation" (2021). *University Honors Theses.* Paper 1036.
https://doi.org/10.15760/honors.1062

Functional role of the N-terminal domain in connexin 46/50 by *in silico* mutagenesis and molecular dynamics simulation

by

Umair Khan

An undergraduate honors thesis submitted in partial fulfillment of the

requirements for the degree of

Bachelor of Science

in

University Honors

and

Computer Science & Mathematics

Thesis Advisor

Steve L. Reichow

Portland State University

2021

Abstract

Connexins form intercellular channels known as gap junctions that facilitate diverse physiological roles, from long-range electrical and chemical coupling to nutrient exchange. Recent structural studies on Cx46 and Cx50 have defined a novel and stable open state and implicated the amino-terminal (NT) domain as a major contributor to functional differences between connexin isoforms. This thesis presents two studies which use molecular dynamics simulations with these new structures to provide mechanistic insight into the function and behavior of the NTH in Cx46 and Cx50. In the first, residues in the NTH that differ between Cx46 and Cx50 are swapped between the two isoforms to identify the particular positions that form the key structural and energetic barriers of ion permeation. In the second, a known cataract-associated mutation is modeled and simulated in Cx50, demonstrating potential atomic interactions with the NTH that could lead to the observed disease phenotype. Together, these studies deepen the field's knowledge of the role of the connexin NT domain, with novel atomic-level detail, and demonstrate how simulation can be combined with experimental methods to better understand the interplay between gap junction structure and function.

Keywords

connexin, gap junction, molecular dynamics, N-terminal domain, cataract

Table of Contents

I. Introduction

Gap junctions are specialized proteins that establish intracellular channels for direct cell-to-cell communication, with 21 isoforms (in humans) known as connexins (Goodenough & Paul, 2009; Sáez et al., 2003). These proteins are fundamental to diverse physiological processes – from synchronizing the beating of heart cells to transmitting electrical signals in the brain – and are critical for long-range communication across nearly every tissue in the body. Mutations in the connexin genes are linked to a wide variety of afflictions, including deafness, skin disease, blindness, heart disease, and neurological disorders (Aasen et al., 2016; Delmar et al., 2018; García et al., 2016). Understanding how these mutations affect the structure (and thereby function) of the associated channels is therefore a key area of gap junction research.

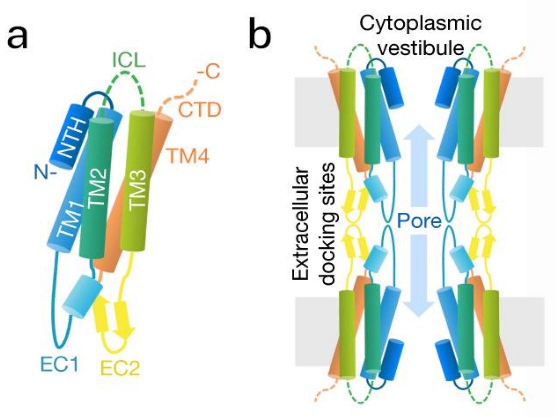

Figure 1. Basic structure of the connexin protein. (a) A single subunit with labeled domains. Dashed lines indicate disordered regions. (b) A full gap junction, with gray bars representing the lipid bilayers of the coupled cells. Figure adapted from Myers et al. (2018).

All connexin isoforms share a similar basic structure (Figure 1) (Beyer & Berthoud, 2017; Grosely & Sorgen, 2013; Sosinsky & Nicholson, 2005). Each connexin subunit is comprised of an N-terminal helical domain (NTH), four transmembrane domains which are embedded in the cell membrane (TM1-4), and two extracellular loops (EC1-2) which stretch outside the cell. There is also an intracellular loop (ICL) connecting TM2 and TM3, and a C-terminal domain (CTD), both of which are believed to be intrinsically disordered regions which reside within the cytosol. Six connexin subunits assemble into a hemichannel, and two hemichannels from neighboring cells dock to form a full dodecameric gap junction.

The NTH is of particular interest in this structure since it extends into the channel pore and is therefore positioned to directly impact permeation and play a key role in channel gating (*i.e.*, opening and closing). Changes to the structure and behavior of the NTH, either through genetic mutation or induced through interactions with other proteins, have been shown to significantly impact the function of gap junctions (Musa et al., 2004; Oh et al., 2004; Peracchia & Peracchia, 2005; Purnick et al., 2000; Srinivas et al., 2005; J.-J. Tong et al., 2004; J.-J. Tong & Ebihara, 2006; Verselis et al., 1994; Xin et al., 2010; Xin & Bai, 2013).

Recently, advancements in single-particle cryo-electron microscopy (CryoEM) have led to new high-resolution structures of two connexin isoforms in particular: connexin-46 (Cx46) and connexin-50 (Cx50) (Flores et al., 2020; Myers et al., 2018). These isoforms are expressed primarily in the eye lens, where proper mediation of the intercellular flow of nutrients and metabolic waste products is crucial for maintaining the optical properties necessary to maintain transparency in this avascular organ (Mathias et al., 2010). Many mutations of Cx46 and Cx50 are associated with congenital cataract formation (or loss of lens transparency) – indeed, Cx50 contains the most cataract-associated mutations of any protein in the lens (Beyer et al., 2013; Shiels et al., 2010). The new models show for the first time a stable open-state conformation of the NTH and provide a strong baseline for structural investigation of this domain, as compared to a previously-solved model of Cx26 (Maeda et al., 2009).

Connexins and their surrounding environment are not static, however, and fixed atomic models can only provide limited insight into the true characteristics of gap junctions. Molecular dynamics (MD) simulation presents a solution to this problem, wherein protein structures can be placed in model cellular

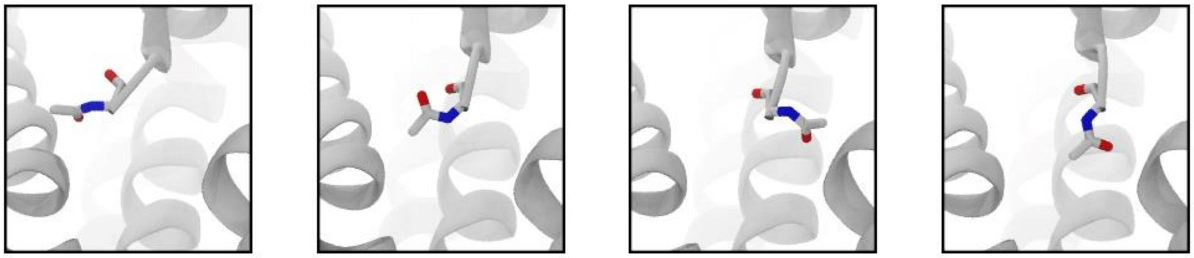

Figure 2. Snapshots of G2 adopting a wide range of conformations at various timepoints in a simulation of Cx50. These behaviors could not be captured in the ensemble CryoEM models.

environments and their behaviors simulated according to the laws of physics and statistical mechanics (Karplus, 2003). These simulations capture the dynamic behavior of the protein at an atomic level that is otherwise unseen in the static model (Figure 2). Furthermore, simulation data can be analyzed to extract quantitative structural, kinetic, and thermodynamic properties, like dihedral angles, interaction distances and dwell times, and free energy comparisons.

In this thesis, *in silico* mutagenesis, in which mutations are modeled into known protein structures, is combined with MD simulation to provide mechanistic insight into the function and behavior of the NTH in Cx46 and Cx50. Two separate studies are described. In the first, residues in the NTH that differ between Cx46 and Cx50 are swapped between the two isoforms to identify the particular positions that form the key structural and energetic barriers of ion permeation (Yue and Haddad et al., 2021). In the second, a known cataract-associated mutation is modeled and simulated in Cx50, demonstrating potential atomic interactions with the NTH that could lead to the observed disease-state phenotype of the channel (Tong and Khan et al., in preparation).

The remainder of this thesis is organized as follows. Chapter II details the usage of modeling and simulation tools along with analysis techniques applied to generate and interpret simulation results. Chapters III and IV discuss the findings of the two studies previously outlined. Chapter V provides an overall summary and briefly considers some of the broader implications of the techniques and results described in the previous chapters.

II. Methods

Material adapted from Yue and Haddad et al. (2021) and Tong and Khan et al. (in preparation).

Visual Molecular Dynamics (VMD) v.1.9.3 was used to build the dodecameric channels for Cx46 (PDB: 6MHQ) and Cx50 (PDB: 6MHY, 7JJP) wildtype systems for molecular dynamics (MD) simulations (Flores et al., 2020; Humphrey et al., 1996; Myers et al., 2018). Sidechains were protonated according to neutral conditions, and the protonated HSD model was used for all histidine residues. Disulfide bonds identified in the experimental structures were enforced for both models. Amino acids corresponding to the ICL and CTD were not included, as experimental data describing the structure of these disordered domains are missing. The introduced N- and C-terminal residues resulting from the missing ICL (L97 and L142 in Cx46; V97 and L154 in Cx50 [6MHY]; R109 and R149 in Cx50 [7JJP]) were neutralized. NT acetylation sites were introduced in VMD through an all-atom acetylation patch using the AutoPSF plugin, to mimic the in vivo co-translational modification identified in the native proteins (Myers et al., 2018; Wang & Schey, 2009).

The four models of the NTH variants (Cx46-R9N, Cx46-50NT, Cx50-N9R and Cx50-46NT) were built by mutating the respective wildtype models with VMD's *mutator* plugin (Humphrey et al., 1996), as per the sequence differences of the NT domain (defined as residue 2 – 19). The T39R mutation was introduced using two separate techniques, to allow comparison of different starting conformations. The *mutator* plugin was used to create a "naïve" model, where arginine was placed in the exact same conformation as the threonine it replaced (referred to as Model 1). SWISS-MODEL (Waterhouse et al., 2018) was then used on the wildtype Cx50 [7JJP] template to generate a mutant homology model with a minimized initial conformation (referred to as Model 2).

The resulting structures were then merged with 1-palmitoyl-2-oleoyl-sn-glycero-3-phosphocholine (POPC) lipid bilayers generated by CHARMM-GUI (Wu et al., 2014) using VMD's *mergestructs* plugin, mimicking a cell-to-cell junction. Lipids that overlapped with the protein and the pore were removed, and the systems were placed in water boxes using VMD's *solvate* plugin. Water that overlapped with the lipid bilayers was then removed. The NTH systems had final dimensions of 150 × 150 × 180 Å, whereas the T39R systems were further trimmed to create hexagonal boundary conditions with circumradius 70 Å and height 200 Å. All systems were then neutralized using the *autoionize* plugin, followed by the addition of 150 mM KCl and 150 mM NaCl to the solvent areas corresponding to intracellular and extracellular regions of the simulation box, respectively. Hydrogen mass repartitioning was applied to both T39R systems to enable a 4 fs timestep (Balusek et al., 2019).

Nanoscale Molecular Dynamics (NAMD) (Phillips et al., 2005, 2020) was used for all classical molecular dynamics (MD) simulations, with the CHARMM36 force field (Huang & MacKerell, 2013) for all atoms and TIP3P explicit model for water. Periodic boundary conditions were used to allow for the particle mesh Ewald calculation of electrostatics. All systems were prepared following a minimization and equilibration protocol, as follows. First, the lipid tails were allowed to minimize with all other atoms fixed for 1 ns using a 1 fs timestep, allowing the acyl chains to "melt" with constant volume at a temperature of 300 K (NVT). All subsequent simulations were performed using the Langevin piston Nosé-Hoover method for pressure control (NPT). Next, the entire system, including lipids, solvent, and ions, was allowed to minimize with the protein harmonically constrained (1 kcal mol^{-1}). The NTH variant systems were simulated for 1 ns with a 1 fs timestep, whereas the T39R systems were simulated for 2 ns with a 2 fs timestep. Further 1 ns / 1 fs and 2 ns / 2 fs minimization steps were then applied to the NTH variant and T39R systems, respectively, in which the system was free to minimize with a harmonic constraint applied only to the protein backbone (1 kcal mol^{-1}). This ensured stable quaternary structure while sidechains relaxed in their local environment. The entire system was then released from all constraints and subject to all-atom equilibration for 30 ns using a Langevin thermostat (damping coefficient of 0.5 ps^{-1}), with a constant temperature of 310 K and constant pressure of 1 atm, using a 2 fs timestep for the NTH variant systems and 4 fs timestep for the T39R systems. After equilibration was complete, each of NTH variant systems was simulated for 25 ns of production with a 2 fs timestep, with four replicates per system to facilitate statistical analysis. The T39R systems were simulated in triplicate for 100 ns production runs, with a 4 fs timestep. All replicas of all systems started from the end of the 30 ns equilibration step with velocities reinitialized.

Root mean squared deviations (r.m.s.d.), comparing the backbone conformations of MD simulation to the original starting structures, and root mean square fluctuations (r.m.s.f.), comparing the amplitudes of backbone fluctuations during MD simulation, were calculated using VMD. All systems approached a steady r.m.s.d. during the equilibration phase and maintained stability during all production runs.

In the NTH variant systems, population distribution functions were constructed by monitoring the distance between residues at the 9th and 12th positions in adjacent subunits (in the clockwise direction when viewed from the cytoplasmic vestibule). Distances between functional groups were recorded at every tenth step of the trajectory across all four production runs, for each of the wildtype and variant systems. The points of reference used to measure the interatomic distance were chosen to capture equivalent rotameric states, as follows: C_ζ for R9, C_γ for N9, and C_δ for E12. Histograms (bin size = 0.1 Å) were normalized and plotted as probability density functions (Figure 3g-h).

Potentials of mean force (PMF), or energy landscapes, describing the permeation of K^+ and Cl^- were calculated for the NTH variant systems (Figure 4b-d). A Markov State Model (MSM) (Pande et al., 2010) was constructed by defining the state-space as the position of an ion along the pore-axis (z-axis), which was subdivided into 3 Å bins. A transition matrix (T), which describes the time evolution of the system, was constructed from the conditional probabilities T_{ij} of an ion starting in state i and ending in state j after a given lag-time. As in previous work (Myers et al., 2018), a short lag-time of 2 ps was used to ensure the vast majority of transition probabilities occurred between nearest neighbors (i.e., $i - 1 \leftrightarrow i \leftrightarrow i + 1$). The principle of detailed balance guarantees that any connected pairing of states (e.g., neighbors) is sufficient to determine the unique equilibrium distribution independent of lag time. Transition probabilities were estimated by counting the instances of transitions at every lag time and storing the values in a transition count matrix. The count matrix was then row normalized to achieve an approximate transition probability matrix (T)

$$T_{i,i+1} \cong \frac{N_{i,i+1}}{N_i} \tag{1}$$

where $N_{i,i+1}$ is the number of transitions from state i to state i + 1 in a lag time of τ = 2 ps, and N_i is the number of times an ion was found in state i. The thermodynamics underlying ionic permeation are then calculated using the principle of detailed balance (3) and Boltzmann statistics (4).

$$P_i^{\mathrm{eq}}\, T_{i,i+1} = P_{i+1}^{\mathrm{eq}}\, T_{i+1,i} \tag{3}$$

$$e^{\frac{-\Delta G_{i,i+1}}{RT}} = \frac{P_{i+1}^{\mathrm{eq}}}{P_i^{\mathrm{eq}}} = \frac{T_{i,i+1}}{T_{i+1,i}} \tag{4}$$

$$\mathrm{PMF}(i) = \sum_{n=1}^{i-1} \Delta G_{n,n+1} = -\sum_{n=1}^{i-1} RT \ln\left(\frac{T_{n,n+1}}{T_{n+1,n}}\right) \tag{5}$$

Here, P_i^{eq} is the probability that an ion will be in each respective bin once equilibrium is achieved, $\Delta G_{i,i+1}$ is the free energy difference between the two states, R is the ideal gas constant (1.986 cal mol^{-1} K^{-1}), and T is temperature (310 K) (5). Values from the PMF were mapped to the z-axis, interpolated and smoothed using a b-spline. Final PMFs were symmetrized around the center of the channel and adjusted such that the bulk regions were at zero. To enable sufficient sampling of Cl$^-$ ions in the channel, a distributed seeding approach was implemented where an individual Cl$^-$ is randomly placed within the channel, followed by a short 10 ns simulation. This process was repeated until sufficient sampling for the MSM was achieved. Further explanation and a detailed justification of the distributed seeding approach, and PMF calculation can be found in (Myers et al., 2018).

Coulombic surface potentials were calculated for the NTH variant systems using the Adaptive Poisson Boltzmann Solver (APBS) within Chimera (Jurrus et al., 2018; Pettersen et al., 2004), using standard settings (Figure 4a). Pore profile analysis of the radius at each point along the pore-axis (Z-axis) was performed with HOLE program (Smart et al., 1996), which rolls a sphere over the Van der Waals surface of the pore (Figure 3a-b). To assess the average pore profile of each model obtained by MD simulation, a snapshot of the protein was saved every 2 ns, symmetrized, and then averaged together.

In the T39R systems, interactions introduced by the mutation were assessed by recording residues within 4 Å of R39 every 10 ps, and aggregating counts across chains and replicates. Once key residues were identified, the distances between each R39 and the residues of interest were recorded every 10 ps across all replicates of all production runs. The points of reference for R39 (C_ζ), D3 (C_γ), and E42 (C_δ) were chosen to capture equivalent rotameric states. Since the acetylated G2 has two oxygen atoms, either of which can interact with R39, the minimum of the distances between R39 and the oxygen atoms was recorded as the distance to G2. Histograms (bin size ≈ 0.1 Å) and corresponding empirical distribution functions (ECDFs) were then plotted (Figure 7b, Figure 8b).

Based on the distance histograms, 4.5 Å was chosen as the cutoff distance below which R39 and another residue were considered to be interacting. This criterion was used to generate time series of binary interaction states for each R39 and each contact residue, recorded every 10ps. Dwell times were obtained by calculating the length of consecutive interaction states, ignoring periods of noninteraction that lasted less than 500 ps (Figure 7c, Figure 8c). Any interactions with a final length of less than 1 ns were ignored. Histograms (bin size = 4 ns) and corresponding ECDFs were then plotted (Figure 7d, Figure 8d).

III. Cx46 and Cx50 channel properties are shaped by structural and dynamic features of their N-terminal domains

> *Material adapted from Yue and Haddad et al. (2021). MD simulation studies in this chapter were carried out in collaboration with Bassam Haddad (Reichow Laboratory). Functional studies were conducted by the laboratory of Dr. Donglin Bai (Western University, Ontario).*

Pore profile analysis of constructed NT-swapped chimeras and single point variants at position 9 of Cx46 and Cx50 shows the resulting models produced pore constriction sites as expected based on the identity of position 9, with some differences resulting from the precise conformation selected by the modeling program for the position 9 variants (Figure 3a). Following simulation, however, the pore profiles of all constructs were modified within the NT domains as compared to their starting structures (Figure 3b), primarily through reorientation of pore-lining sidechain residues. In contrast to the experimental starting models, the ensemble of structures obtained by MD displayed averaged steric landscapes that were all very similar to each other. Cx50, Cx46-50NT and Cx46-R9N all converged to a similar profile, with a primary constriction site diameter of ~9.2 – 9.6 Å that is substantially smaller than the experimental model of Cx50 and defined primarily by S5/D3. In comparison, Cx46, Cx50-46NT and Cx50-N9R all converged to a similar profile that is larger than the experimental model of Cx46, ranging from ~9.7 Å for Cx46 and Cx50-N9R to ~10.9 Å for Cx50-46NT.

In contrast to the starting structures, the R9 position is no longer contributing as the primary constriction site in the MD averaged models. Upon closer inspection, it is observed that R9 adopts a dynamic exchange of conformational states during simulation of Cx46, Cx50-46NT and Cx50-N9R, which reorients the sidechain away from the pore permeation pathway (Figure 3c-f). These conformations include the formation of a salt bridge between the positively charged R9 sidechain and the negatively charged E12 position (heavy atom distance = 2.6 Å) of a neighboring subunit at the i + 1 position, which is a conserved site in all models (Figure 3e). Amongst the three variants containing an arginine at position 9, this interaction accounts for ~30-50% of the conformational states observed by MD (Figure 3g). An alternative,

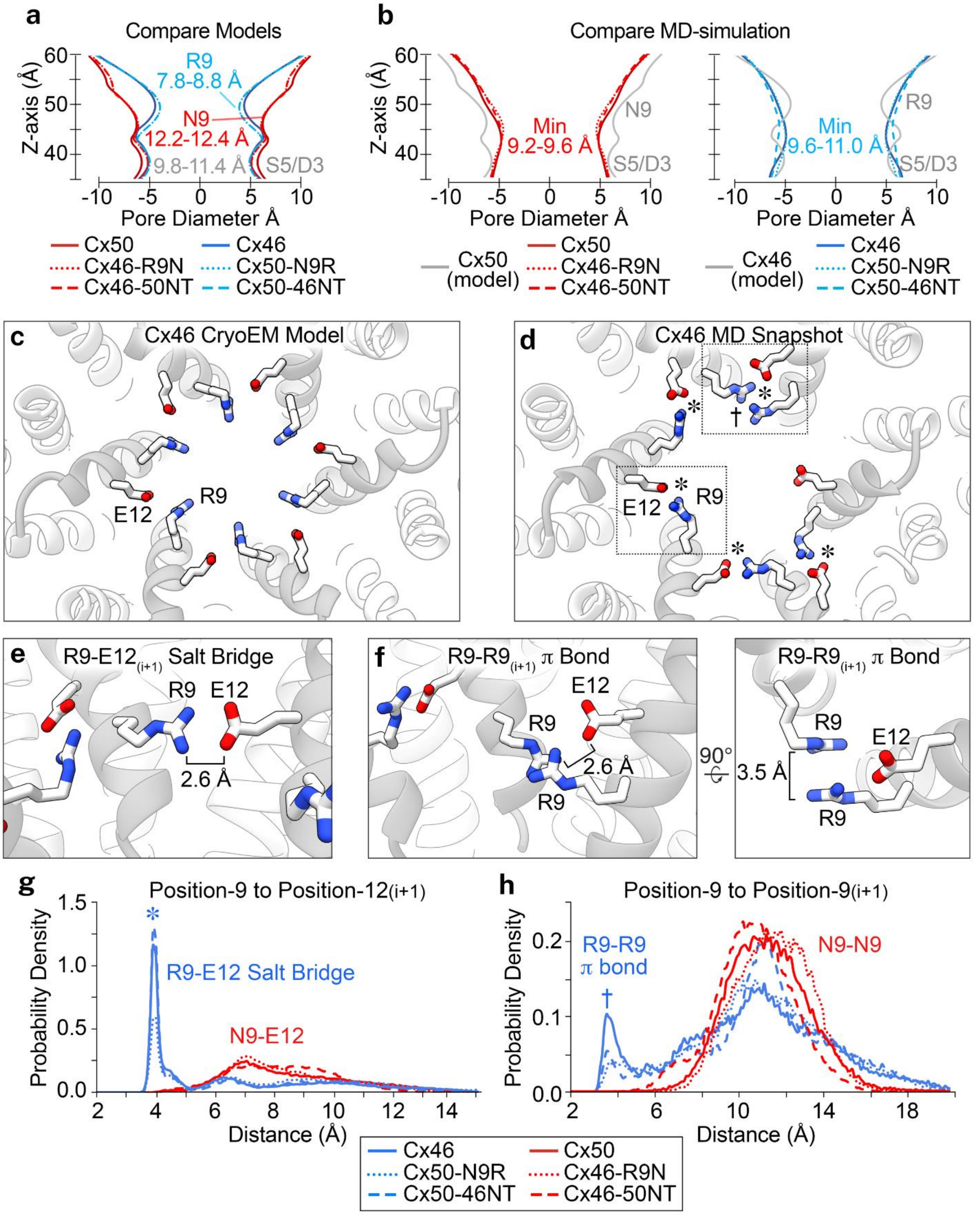
a
Compare Models
Z-axis (Å)
60
50
40
R9
7.8-8.8 Å
N9
12.2-12.4 Å
9.8-11.4 Å
S5/D3
-10
-5
0
5
10
Pore Diameter Å
Cx50
Cx46-R9N
Cx46-50NT
Cx46
Cx50-N9R
Cx50-46NT
b
Compare MD-simulation
Z-axis (Å)
60
50
40
Min
9.2-9.6 Å
N9
S5/D3
-10
-5
0
5
10
Pore Diameter Å
Cx50 (model)
Cx50
Cx46-R9N
Cx46-50NT
R9
Min
9.6-11.0 Å
S5/D3
-10
-5
0
5
10
Pore Diameter Å
Cx46 (model)
Cx46
Cx50-N9R
Cx50-46NT
c
Cx46 CryoEM Model
R9
E12
d
Cx46 MD Snapshot
*
†
E12
R9
e
R9-E12(i+1) Salt Bridge
R9
E12
2.6 Å
f
R9-R9(i+1) π Bond
E12
R9
2.6 Å
R9
90°
R9-R9(i+1) π Bond
R9
E12
3.5 Å
R9
g
Position-9 to Position-12(i+1)
Probability Density
1.5
1.0
0.5
0.0
*
R9-E12 Salt Bridge
N9-E12
2
4
6
8
10
12
14
Distance (Å)
h
Position-9 to Position-9(i+1)
Probability Density
0.2
0.1
0.0
R9-R9
π bond
†
N9-N9
2
6
10
14
18
Distance (Å)
Cx46
Cx50-N9R
Cx50-46NT
Cx50
Cx46-R9N
Cx46-50NT

Figure 3 (previous page). Constriction sites are augmented following MD equilibration, with R9 adopting a dynamic ensemble of stable conformational states that prevent pore constriction. (a) Pore diameter analysis of Cryo-EM based structures of wildtype and variants. (b) Averaged pore diameter of following MD equilibration (pore profile of the starting structures from are shown for comparison in grey). (c) Structure of Cx46 viewed along the pore axis with residues R9 and E12 displayed in stick representation. R9 is oriented toward the center of the pore, forming a primary constriction site. (d) Representative snapshot of Cx46 following MD equilibration. R9 adopts alternative conformational states that reorient the sidechain away from the pore permeation pathway, stabilized by salt bridge interactions with a neighboring E12 (asterisk, ∗) and/or π-π interactions with R9 from a neighboring subunit (dagger, †). (e) Zoom view of a representative R9 salt bridge interaction with a neighboring E12 residue. (f) Zoom view of a representative π-π interaction between two R9 residues of neighboring subunits. (g) Probability distribution of the distance between position 9 to position 12 in the neighboring subunit obtained from MD simulation for Cx46, Cx50-N9R and Cx50-46NT (blue traces) and Cx50, Cx46-R9N and Cx46-50NT (red traces). (h) Probability distribution of the distance between position 9 and position 9 in the neighboring subunit obtained from MD simulation for Cx46, Cx50-N9R and Cx50-46NT (blue traces) and Cx50, Cx46-R9N and Cx46-50NT (red traces). Figure adapted from Yue and Haddad et al. (2021).

and less populated, conformational state is also observed, where R9 forms an optimal π-π stacking interaction with the guanidinium group of a neighboring R9 (planar distance = 3.5 Å) from an adjacent subunit at the i + 1 position (Figure 3f). This state appears to be further stabilized by salt bridge formation between R9 and E12 of the same subunit, or between neighboring subunits. This conformation was observed in ~5-10% of the total conformational states observed by MD (Figure 3h). In all cases, these bridging interactions effectively withdraw the large R9 sidechain away from the permeation pathway and stabilize R9 against the lumen of the channel. Equivalent interactions were not observed in variants where position 9 is occupied by asparagine, with N9 appearing to adopt more random (fluctuating) conformational states (Figure 3g-h).

Given the similarities between Cx50 and Cx46 pore constriction sites observed by MD, the next goal was understanding how position 9 and the NT domain may contribute to differences in their respective

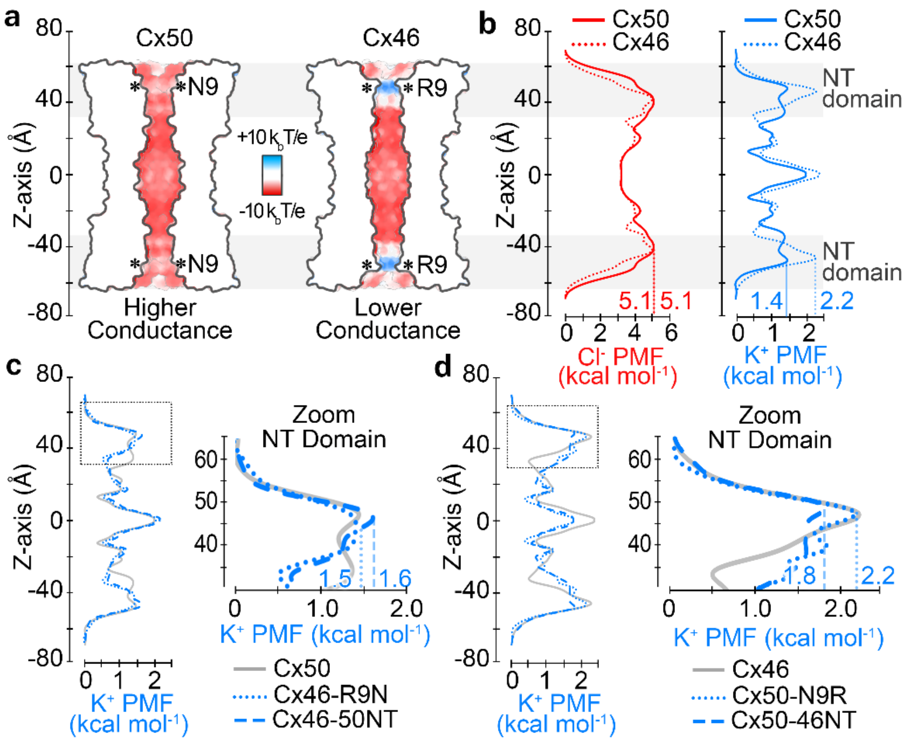

Figure 4. Electrostatics and energetics of the ion permeation pathways of Cx50, Cx46 and NT variants. (a) Cut-away surface representation of Cx50 and Cx46, colored by Coulombic potential (red, negative; white, neutral; blue, positive). (b) Potential of mean force (PMF) describing the free-energy landscape (ΔG) experienced by Cl- ions (red traces) and K+ ions (blue traces) permeating the channel pore of Cx50 and Cx46, as compared to the bulk solvent. (c) PMFs of K+ ions for designed variants Cx46-R9N and Cx46-50NT, with PMF for Cx50 displayed for comparison (gray trace). (d) PMFs of K+ ions for designed variants Cx50-N9R and Cx50-46NT, with PMF for Cx46 displayed for comparison (gray trace). PMFs were symmetrized along Z-axis, and peak energetic barriers identified within the NT domains are indicated. Figure adapted from Yue and Haddad et al. (2021).

energetic barriers to ion permeation, by evaluating the potential of mean force (PMF) for Cl^- and K^+. Note that inspection of the Coulombic surface of the Cx50 starting model shows that this isoform lacks any positive charge within the pore when the NT is acetylated (Figure 4a). In contrast, Cx46 possesses a prominent ring of positive Coulombic potential, belonging to R9, that lines the cytoplasmic vestibules at both ends of the channel. The Coulombic surface potentials of the resulting mutation models are similar to their wildtype counterparts based on the presence or absence of an arginine at the 9th position.

Consistent with their Coulombic surface properties, the MD-derived PMFs for Cl- showed a large peak energetic barrier, ΔG_{Cl-} ~5.1 kcal mol^{-1} for both Cx50 and Cx46 (defined as the difference between bulk solvent and peak PMF barrier to Cl^{-}), which is at least twice as high as the peak energetic barriers to K^{+} (Figure 4b). The primary energetic barriers to both Cl^{-} and K^{+} is established within the NT region of the channels, which is consistent with this domain acting as the selectivity filter and with the displayed preference for cations that has been previously demonstrated experimentally for both Cx50 and Cx46 (Sakai et al., 2003; Srinivas et al., 1999; X. Tong et al., 2014; Trexler et al., 1996). The analysis of energetic differences was therefore focused on K^{+} (the major permeant ion).

The most distinct energetic differences between Cx50 and Cx46 correspond to the region of the NT domain that aligns with position 9, where Cx46 has a peak energy barrier to K^{+} of ~2.24 kcal mol^{-1} and Cx50 has a peak barrier of ~1.42 kcal mol^{-1}, values that agree with previous simulation work (Myers et al., 2018). The difference in peak K^{+} PMF barriers in these two models ($\Delta\Delta G_{K+}$ = 0.82 kcal mol^{-1}) is expected to be primarily due to the positive charge characteristics of R9, and not local differences in channel diameter, as suggested by the previous analysis of the channel pore profile.

The K^{+} ion PMF profiles for the variants show that replacing the entire NT domain of Cx46 with that of Cx50 (Cx46-50NT) or the 9th residue (Cx46-R9N) substantially reduced or eliminated the differences in NT domain energy barriers, as compared to Cx46 ($\Delta\Delta G_{K+}$ = 0.03 – 0.2 kcal mol^{-1}), by effectively reducing the peak barrier around the 9th position (Figure 4c). Likewise, replacing the entire NT domain of Cx50 with that of Cx46 (Cx50-46NT) or the 9th residue (Cx50-N9R) also reduced the energy difference between Cx46 and Cx50 ($\Delta\Delta G_{K+}$ = 0.04 – 0.4 kcal mol^{-1}), this time by increasing the peak barrier to a level similar to Cx46 (Figure 4d). Notably, although the K^{+} energy barrier obtained for Cx50-46NT (ΔG_{K+} = 1.82 kcal mol^{-1}) is significantly larger than that of wildtype Cx50, it remains lower than that of Cx46 and Cx50-N9R. This difference is proposed to reflect the larger pore diameter of this model, resulting in a less constrictive environment for ion permeation. Taken together, these data confirm that the primary

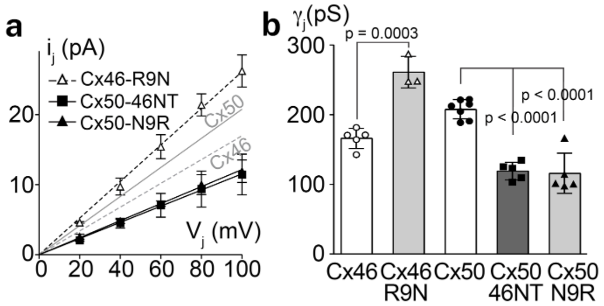

Figure 5. Comparing conductance of Cx46, Cx50, and NT variants. (a) The amplitude of i_j for the main open state at each tested V_j is plotted against V_j. The slope γ_j of Cx46-R9N is 261 ± 6 pS (n = 3), Cx50-N9R γ_j is 122 ± 3 pS (n = 5), and Cx50-46NT γ_j is 116 ± 5 pS (n = 5). (b) Bar graph to summarize the slope γ_js of all tested variants. The γ_j of Cx46-R9N was significantly higher than that of Cx46 and the γ_js of Cx50-46NT and Cx50-N9R were significantly lower than that of Cx50 (one-way ANOVA followed by Tukey's post hoc test). Figure adapted from Yue and Haddad et al. (2021).

difference in K^+ energy barriers between Cx46 and Cx50 is due to the placement of a positively charged arginine at the 9th position.

To investigate the functional effects of this positively charged residue and correlate MD simulation results with experimental data, sheep Cx46, Cx50, and designed NT variants were expressed in GJ-deficient N2A cells *(performed by the laboratory of Dr. Donglin Bai, Western University, Ontario)*. Cell pairs with trafficked GJs were voltage clamped using dual whole cell patch clamp technique (Veenstra, 2016). The unitary conductance (γ_j) of Cx46, Cx50, and the designed NT domain variants was characterized based on single channel current (i_j) recordings at varying voltage (V_j) values. The averaged i_js were plotted at different V_js and a linear regression i_j-V_j plot was used to estimate the slope unitary channel conductance (γ_j). The γ_j of Cx46 was found to be 170 ± 3 pS, whereas the γ_j of Cx50 was 208 ± 3 pS. In comparison, Cx46-R9N GJs showed a significant increase in slope γ_j (261 ± 6 pS) from that of wildtype Cx46 GJ. Conversely, Cx50-N9R GJs displayed a significantly decreased slope γ_j (122 ± 3 pS) than that of wildtype Cx50 GJ. Replacing the NT domain of Cx50 with that of Cx46 (Cx50-46NT) also resulted in a more pronounced drop in slope γ_j (116 ± 5 pS). The slope single channel conductance values of all tested variants were then plotted as a bar graph for direct comparison. These effects are qualitatively consistent with the predicted results obtained by MD, though the placement or removal of R9 had a surprisingly higher degree of effect than expected, with channel variants having correspondingly higher or lower unitary conductance as compared to wildtype channels.

IV. Effect of a cataract-associated mutation on open-state stability of Cx50

> *Material adapted from Tong and Khan et al. (in preparation). MD simulation studies in this chapter were carried out in collaboration with Bassam Haddad (Reichow Laboratory). Functional studies were conducted by the laboratory of Dr. Lisa Ebihara (Rosalind Franklin University).*

In initial functional experiments *(performed by the laboratory of Dr. Lisa Ebihara, Rosalind Franklin University)*, *Xenopus* oocytes were injected with 2 ng of T39R or Cx50 cRNA and incubated in Modified Barth's Solution in the presence or absence of external calcium. In the absence of external calcium, most of T39R cRNA-injected oocytes developed cell blebbing, cytoplasm leakage, and pigmentation changes consistent with cell death by 24 hours after injection (Figure 6a). In contrast, Cx50 cRNA-injected oocytes and antisense-injected control oocytes (AS) remained healthy without any obvious changes in membrane pigmentation. The survival time of the T39R expressing oocytes could be significantly prolonged by incubating the oocytes in external medium containing 3 mM $[Ca^{2+}]_o$. Less than 5% of control and Cx50-injected oocytes died by 48 hours when incubated in the absence or presence of calcium. In contrast, 98% and 25% of T39R-injected oocytes died by 48 hours when incubated in the absence or presence of calcium, respectively (Figure 6b).

One explanation for these findings is that T39R channels exhibit enhanced hemichannel activity that could be partially blocked by increasing external calcium. To investigate this possibility, oocytes were injected with extremely low concentrations of mutant mRNA (0.05 – 0.25 ng) that were insufficient to induce cell death and studied at times ranging between 18 – 72 hours after injection using a two-electrode-voltage-clamp technique. Oocytes injected with 0.25 ng of T39R cRNA exhibited large hemichannel currents that could be partially blocked by raising $[Ca^{2+}]_o$ from nominally zero to 2 mM. In contrast, oocytes injected with 1 – 20 ng Cx50 cRNA or antisense-treated control oocytes showed little or no calcium sensitive hemichannel currents consistent with the results of previous studies (Figure 6c-e) (Minogue et al., 2009; J.-J. Tong et al., 2013).

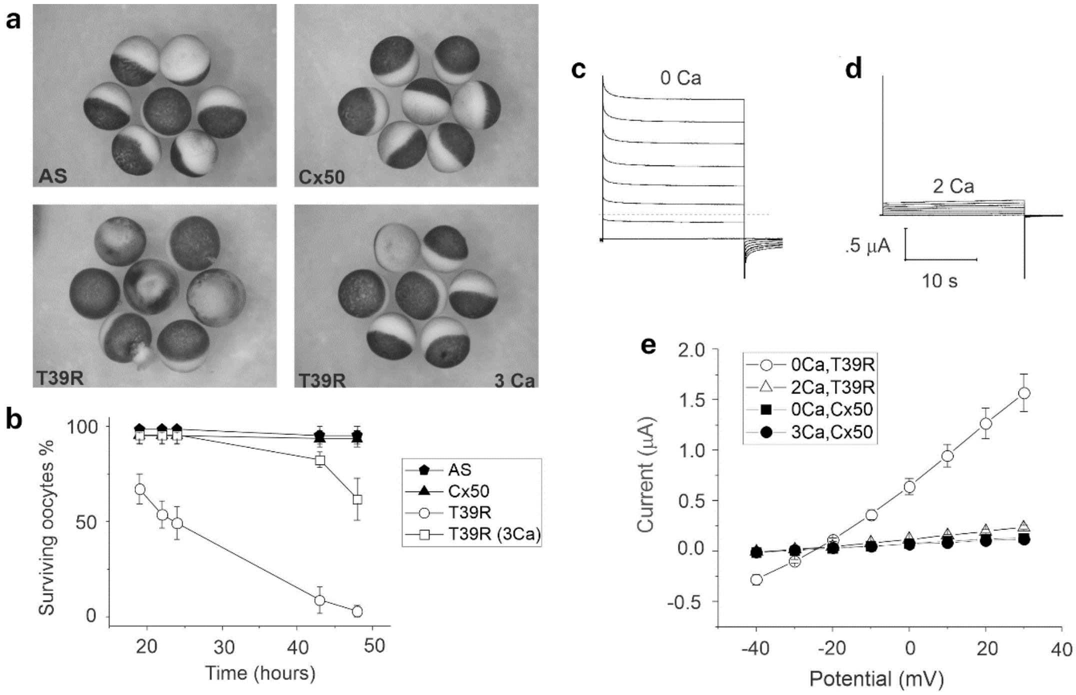

Figure 6. T39R has a toxic effect on oocytes that can rescued by increasing external calcium. (a) Oocytes injected with T39R cRNA show obvious signs of cell death after a 24-hour incubation (bottom left). In contrast, normal cRNA-injected oocytes (Cx50) and antisense-injected control oocytes (AS) remained healthy (top left and right). Raising the external calcium from 1 to 3 mM rescued the T39R-injected oocytes from cell death (bottom right). (b) Graph shows the percentage of surviving oocytes at various times following injection of normal or mutant cRNA. (c, d) Families of current traces recorded from a T39R cRNA-injected oocyte before and after application of calcium, respectively. In the presence of nominally zero calcium, a large hemichannel current was observed. Application of calcium caused a marked reduction in the amplitude of the current at both positive and negative potentials. (e) Steady-state I-V relationships in Cx50 (closed symbols) and T39R (open symbols) cRNA-injected oocytes before and after application of calcium. Figure adapted from Tong and Khan et al. (in preparation).

To gain mechanistic insight toward the gain-of-function observed by T39R, all-atom equilibrium-state MD simulation studies were conducted with multiple replicates (n = 3). T39R models were constructed *in silico* by two independent methods (Model 1 and 2), to allow comparison of different starting conformations (see Chapter II). Contact analysis of R39 in these simulations highlighted a cluster of amino acids that were within interacting distance to the introduced positively charged guanidinium group. The

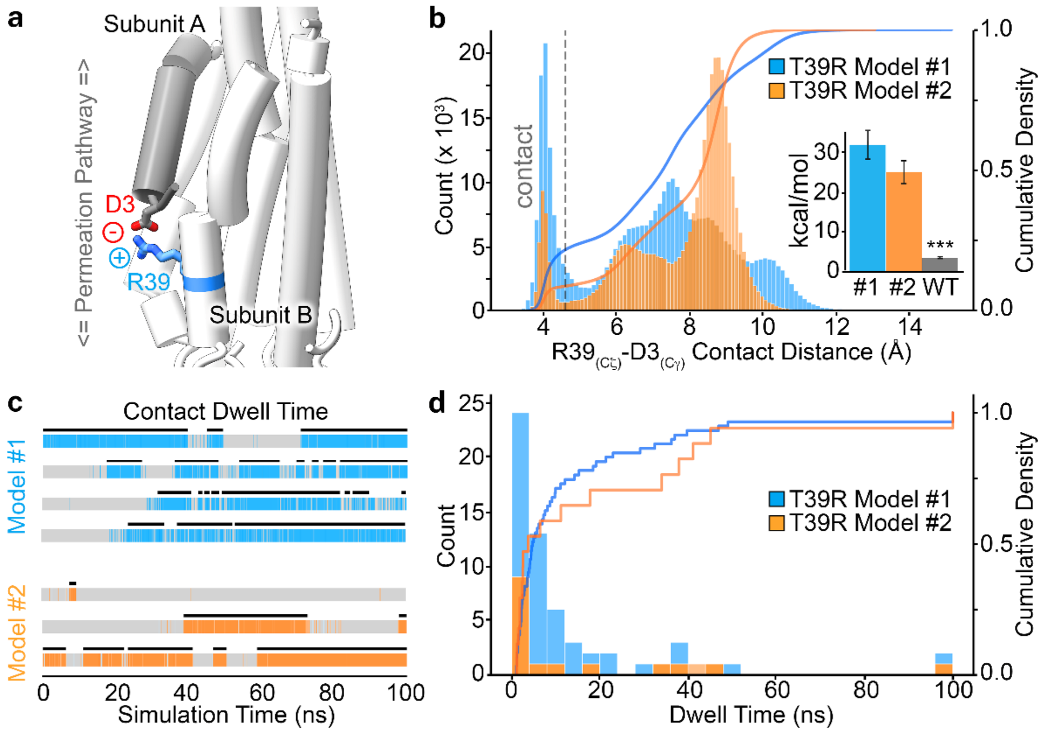

Figure 7. T39R forms a neutralizing salt-bridge interaction with D3. (a) Representative snapshot of an MD trajectory illustrating a salt-bridge interaction between the positively charged R39 and negatively charged residue D3, from a neighboring subunit. (b) Histogram and cumulative density profile showing the population distribution of distance measurements between R39 C_ζ and D3 C_γ. Separation distances less than 4.5 Å are considered to be within contact distance. (c) Dwell time analysis for representative subunit trajectories. Black bars indicate the filtered dwell time in each of the trajectories. (d) Histogram and cumulative density profile showing the population distribution of filtered dwell time measurements. Figure adapted from Tong and Khan et al. (in preparation).

sites with the highest contact frequency were consistent in both MD simulation models and localized to the proximal region of the NT domain, and surrounding residues on TM1. The interactions with the NT domain were localized to residues G2, D3 and W4, while the most significant interaction within TM1 localized to the negatively charged residue E42. Given the role of the NT domain in voltage-sensing and potential coupling between TM1 and voltage-gating response (Peracchia & Peracchia, 2005; Srinivas et al., 2005; J.-J. Tong et al., 2004; J.-J. Tong & Ebihara, 2006; Yue and Haddad et al., 2021), a detailed analysis of these interacting residues was then conducted.

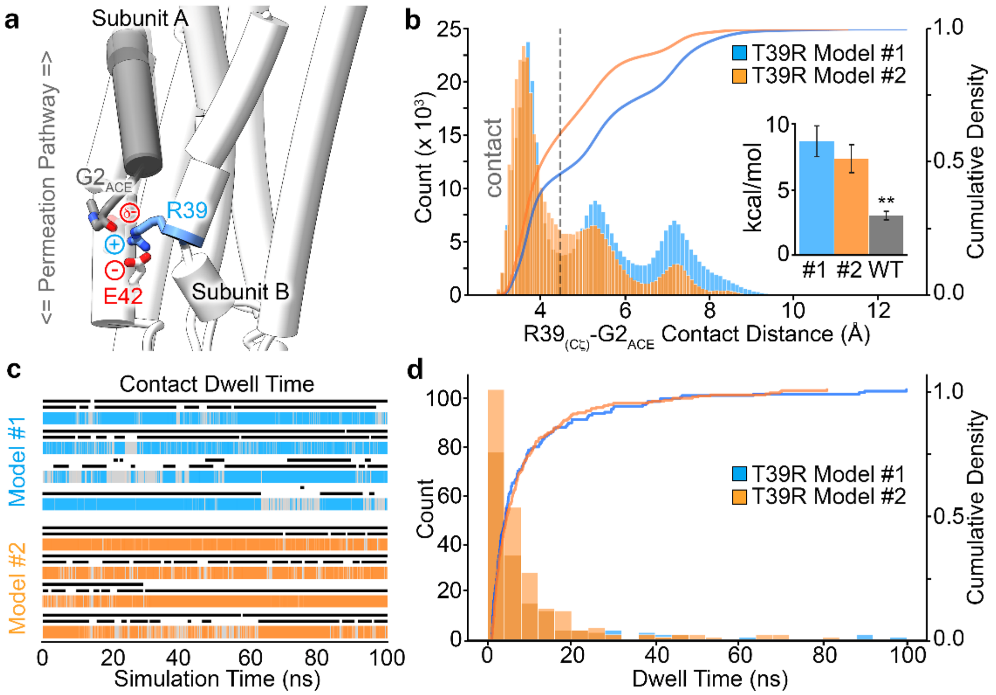

Figure 8. T39R forms a stable interaction with G2 and E42. (a) Representative snapshot of an MD trajectory illustrating a triad interaction between the positively charged R39 and negatively charged residue E42 and acetylated G2 ($G2_{ACE}$), from a neighboring subunit. (b) Histogram and cumulative density profile showing the population distribution of distance measurements between R39 C_{ζ} and carbonyl oxygens on. Separation distances less than 4.5 Å are considered to be within contact distance. (c) Dwell time analysis for representative subunit trajectories. Black bars indicate the filtered dwell time of interaction between R39 and $G2_{ACE}$ (bottom) and E42 (top) in each of the trajectories. (d) Histogram and cumulative density profile showing the population distribution of filtered dwell time measurements for R39-$G2_{ACE}$ interactions. Figure adapted from Tong and Khan et al. (in preparation).

The residue D3, located at the proximal end of the NT domain, has been shown to function as a voltage-sensor in Cx50 (Peracchia & Peracchia, 2005; Srinivas et al., 2005), as well as in other connexin isoforms (Verselis et al., 1994; Xu et al., 2016). Remarkably, in each of the simulations conducted, the large positively charged sidechain of R39 was found to extend toward the negatively charged carboxylate group on D3, located on a neighboring subunit, forming an apparent salt-bridge interaction (Figure 7a). This charge-neutralizing interaction could effectively alter the voltage sensitivity of Cx50, consistent with functional results. To assess the prevalence of this interaction, a contact distance analysis was conducted, which showed that this neutralizing salt-bridge interaction accounts for ~9 – 21% of the conformational states sampled by R39 during MD production period (Figure 6b). Dwell-time analysis of the R39-D3 interaction indicates transient stability, with the majority of interactions lasting < 50 ns, though in a few instances the interaction persisted through the duration of the MD production runs (100 ns) (Figure 6c-d).

R39 also adopts an alternative conformation that facilitates simultaneous interaction with the two partial negative charges presented by the carbonyl oxygens on the acetylated G2 position ($G2_{ACE}$) and the negatively charged residue E42 from a neighboring subunit (Figure 8a). Such an interaction, in particular with G2, could further stabilize the open-state conformation of the NT domain. Contact distance analysis indicates that the interaction between R39 and $G2_{ACE}$ is highly populated, accounting for 46 – 62% of the conformational states adopted by R39 during the MD simulation runs (Figure 8b). The frequency of this interaction was also significant in both MD models, as assessed by dwell time analysis. In comparison to the R39-D3 interaction, the coupling to G2 appears much more frequent and persistent. While the majority of dwell times for the R39-$G2_{ACE}$ interaction are < 50 ns, a number of trajectories displayed interaction dwell times of 50 – 100 ns (Figure 8c-d).

Notably, stabilization of the conformational state supporting the interaction with $G2_{ACE}$ appears to be facilitated by a salt-bridge with E42. Corresponding dwell time analysis of this interaction is overlaid with the G2 interaction in Figure 8C (top black bars). This analysis indicates that R39 interaction with G2 is supported by the salt-bridge interaction with E42; however, it is not a requirement, as analysis of multiple trajectories show that these interactions are not necessarily correlated (compare black bars in Figure 8c).

V. Conclusion

In the first study, R9 was identified as the key energetic barrier to K^+ permeation in Cx46 through site-specific and full NT domain chimeras of Cx50, which was correlated with experimental data showing that channel conductance properties were also swapped in NT variants. Moreover, the MD results demonstrated that this barrier was established due to the positive charge of the sidechain, not by a constriction of the pore from the length of the arginine residue. Instead, the R9 sidechain is oriented away from the center of the pore, relieving any significant steric obstruction, through a pair of inter-subunit interactions with neighboring E12 and R9 residues. These findings add a new level of understanding to previous work which identified the NT domain as the primary determinant of channel selectivity (Musa et al., 2004; Srinivas et al., 2005; J.-J. Tong et al., 2004; Xin & Bai, 2013).

The second study suggests that the T39R mutation in Cx50 causes cataracts by greatly increasing the probability of hemichannel opening. This is hypothesized to occur in part due to introduced interactions with the NTH identified in MD simulations of this mutant, where electrostatic contacts between R39 and the D3 and G2 residues stabilize the NT domain against the pore wall and potentially neutralize the voltage sensor, which ultimately prevents the NT domain from closing the channel. This increase in hemichannel activity would be expected to lead to widespread cell death and the development of total cataract consistent with the mutation phenotype.

As the computational power of hardware increases and novel parallel algorithms are developed, molecular dynamics simulations will be able to provide even deeper insights into the behavior of proteins, going beyond specific short time-scale interactions and moving towards describing in detail complete slow time-scale mechanisms, such as channel gating. Combined with functional and experimental results, studies like these are positioned to provide the field with a new atomic understanding of the interplay between gap junction structure and function.

References

Aasen, T., Mesnil, M., Naus, C. C., Lampe, P. D., & Laird, D. W. (2016). Gap Junctions and Cancer: Communicating for 50 Years. *Nature Reviews. Cancer*, *16*(12), 775–788. https://doi.org/10.1038/nrc.2016.105

Balusek, C., Hwang, H., Lau, C. H., Lundquist, K., Hazel, A., Pavlova, A., Lynch, D. L., Reggio, P. H., Wang, Y., & Gumbart, J. C. (2019). Accelerating membrane simulations with Hydrogen Mass Repartitioning. *Journal of Chemical Theory and Computation*, *15*(8), 4673–4686. https://doi.org/10.1021/acs.jctc.9b00160

Beyer, E. C., & Berthoud, V. M. (2017). Gap junction structure: Unraveled, but not fully revealed. *F1000Research*, *6*. https://doi.org/10.12688/f1000research.10490.1

Beyer, E. C., Ebihara, L., & Berthoud, V. M. (2013). Connexin mutants and cataracts. *Frontiers in Pharmacology*, *4*, 43. https://doi.org/10.3389/fphar.2013.00043

Delmar, M., Laird, D. W., Naus, C. C., Nielsen, M. S., Verselis, V. K., & White, T. W. (2018). Connexins and Disease. *Cold Spring Harbor Perspectives in Biology*, *10*(9). https://doi.org/10.1101/cshperspect.a029348

Flores, J. A., Haddad, B. G., Dolan, K. A., Myers, J. B., Yoshioka, C. C., Copperman, J., Zuckerman, D. M., & Reichow, S. L. (2020). Connexin-46/50 in a dynamic lipid environment resolved by CryoEM at 1.9 Å. *Nature Communications*, *11*(1), 4331. https://doi.org/10.1038/s41467-020-18120-5

García, I. E., Prado, P., Pupo, A., Jara, O., Rojas-Gómez, D., Mujica, P., Flores-Muñoz, C., González-Casanova, J., Soto-Riveros, C., Pinto, B. I., Retamal, M. A., González, C., & Martínez, A. D. (2016). Connexinopathies: A structural and functional glimpse. *BMC Cell Biology*, *17*(Suppl 1). https://doi.org/10.1186/s12860-016-0092-x

Goodenough, D. A., & Paul, D. L. (2009). Gap Junctions. *Cold Spring Harbor Perspectives in Biology*, *1*(1). https://doi.org/10.1101/cshperspect.a002576

Grosely, R., & Sorgen, P. L. (2013). A History of Gap Junction Structure: Hexagonal Arrays to Atomic Resolution. *Cell Communication & Adhesion*, *20*(0). https://doi.org/10.3109/15419061.2013.775256

Huang, J., & MacKerell, A. D. (2013). CHARMM36 all-atom additive protein force field: Validation based on comparison to NMR data. *Journal of Computational Chemistry*, *34*(25), 2135–2145. https://doi.org/10.1002/jcc.23354

Humphrey, W., Dalke, A., & Schulten, K. (1996). VMD: Visual molecular dynamics. *Journal of Molecular Graphics*, *14*(1), 33–38, 27–28. https://doi.org/10.1016/0263-7855(96)00018-5

Jurrus, E., Engel, D., Star, K., Monson, K., Brandi, J., Felberg, L. E., Brookes, D. H., Wilson, L., Chen, J., Liles, K., Chun, M., Li, P., Gohara, D. W., Dolinsky, T., Konecny, R., Koes, D. R., Nielsen, J. E., Head-Gordon, T., Geng, W., … Baker, N. A. (2018). Improvements to the APBS biomolecular solvation software suite. *Protein Science: A Publication of the Protein Society*, *27*(1), 112–128. https://doi.org/10.1002/pro.3280

Karplus, M. (2003). Molecular dynamics of biological macromolecules: A brief history and perspective. *Biopolymers*, *68*(3), 350–358. https://doi.org/10.1002/bip.10266

Maeda, S., Nakagawa, S., Suga, M., Yamashita, E., Oshima, A., Fujiyoshi, Y., & Tsukihara, T. (2009). Structure of the connexin 26 gap junction channel at 3.5 A resolution. *Nature*, *458*(7238), 597–602. https://doi.org/10.1038/nature07869

Mathias, R. T., White, T. W., & Gong, X. (2010). Lens Gap Junctions in Growth, Differentiation, and Homeostasis. *Physiological Reviews*, *90*(1), 179–206. https://doi.org/10.1152/physrev.00034.2009

Minogue, P. J., Tong, J.-J., Arora, A., Russell-Eggitt, I., Hunt, D. M., Moore, A. T., Ebihara, L., Beyer, E. C., & Berthoud, V. M. (2009). A mutant connexin50 with enhanced hemichannel function leads to cell death. *Investigative Ophthalmology & Visual Science*, *50*(12), 5837–5845. https://doi.org/10.1167/iovs.09-3759

Musa, H., Fenn, E., Crye, M., Gemel, J., Beyer, E. C., & Veenstra, R. D. (2004). Amino terminal glutamate residues confer spermine sensitivity and affect voltage gating and channel conductance of rat connexin40 gap junctions. *The Journal of Physiology*, *557*(Pt 3), 863–878. https://doi.org/10.1113/jphysiol.2003.059386

Myers, J. B., Haddad, B. G., O'Neill, S. E., Chorev, D. S., Yoshioka, C. C., Robinson, C. V., Zuckerman, D. M., & Reichow, S. L. (2018). Structure of native lens connexin 46/50 intercellular channels by cryo-EM. *Nature*, *564*(7736), 372–377. https://doi.org/10.1038/s41586-018-0786-7

Oh, S., Rivkin, S., Tang, Q., Verselis, V. K., & Bargiello, T. A. (2004). Determinants of Gating Polarity of a Connexin 32 Hemichannel. *Biophysical Journal*, *87*(2), 912–928. https://doi.org/10.1529/biophysj.103.038448

Pande, V. S., Beauchamp, K., & Bowman, G. R. (2010). Everything you wanted to know about Markov State Models but were afraid to ask. *Methods*, *52*(1), 99–105. https://doi.org/10.1016/J.YMETH.2010.06.002

Peracchia, C., & Peracchia, L. L. (2005). Inversion of both gating polarity and CO2 sensitivity of voltage gating with D3N mutation of Cx50. *American Journal of Physiology. Cell Physiology*, *288*(6), C1381-1389. https://doi.org/10.1152/ajpcell.00348.2004

Pettersen, E. F., Goddard, T. D., Huang, C. C., Couch, G. S., Greenblatt, D. M., Meng, E. C., & Ferrin, T. E. (2004). UCSF Chimera—A visualization system for exploratory research and analysis. *Journal of Computational Chemistry*, *25*(13), 1605–1612. https://doi.org/10.1002/jcc.20084

Phillips, J. C., Braun, R., Wang, W., Gumbart, J., Tajkhorshid, E., Villa, E., Chipot, C., Skeel, R. D., Kalé, L., & Schulten, K. (2005). Scalable molecular dynamics with NAMD. *Journal of Computational Chemistry*, *26*(16), 1781–1802. https://doi.org/10.1002/jcc.20289

Phillips, J. C., Hardy, D. J., Maia, J. D. C., Stone, J. E., Ribeiro, J. V., Bernardi, R. C., Buch, R., Fiorin, G., Hénin, J., Jiang, W., McGreevy, R., Melo, M. C. R., Radak, B. K., Skeel, R. D., Singharoy, A., Wang, Y., Roux, B., Aksimentiev, A., Luthey-Schulten, Z., … Tajkhorshid, E. (2020). Scalable molecular dynamics on CPU and GPU architectures with NAMD. *The Journal of Chemical Physics*, *153*(4), 044130. https://doi.org/10.1063/5.0014475

Purnick, P. E. M., Oh, S., Abrams, C. K., Verselis, V. K., & Bargiello, T. A. (2000). Reversal of the Gating Polarity of Gap Junctions by Negative Charge Substitutions in the N-Terminus of Connexin 32. *Biophysical Journal*, *79*(5), 2403–2415. https://doi.org/10.1016/S0006-3495(00)76485-X

Sáez, J. C., Berthoud, V. M., Brañes, M. C., Martínez, A. D., & Beyer, E. C. (2003). Plasma Membrane Channels Formed by Connexins: Their Regulation and Functions. *Physiological Reviews*, *83*(4), 1359–1400. https://doi.org/10.1152/physrev.00007.2003

Sakai, R., Elfgang, C., Vogel, R., Willecke, K., & Weingart, R. (2003). The electrical behaviour of rat connexin46 gap junction channels expressed in transfected HeLa cells. *Pflugers Archiv: European Journal of Physiology*, *446*(6), 714–727. https://doi.org/10.1007/s00424-003-1129-5

Shiels, A., Bennett, T. M., & Hejtmancik, J. F. (2010). Cat-Map: Putting cataract on the map. *Molecular Vision*, *16*, 2007–2015.

Smart, O. S., Neduvelil, J. G., Wang, X., Wallace, B. A., & Sansom, M. S. P. (1996). HOLE: A program for the analysis of the pore dimensions of ion channel structural models. *Journal of Molecular Graphics*, *14*(6), 354–360. https://doi.org/10.1016/S0263-7855(97)00009-X

Sosinsky, G. E., & Nicholson, B. J. (2005). Structural organization of gap junction channels. *Biochimica Et Biophysica Acta*, *1711*(2), 99–125. https://doi.org/10.1016/j.bbamem.2005.04.001

Srinivas, M., Costa, M., Gao, Y., Fort, A., Fishman, G. I., & Spray, D. C. (1999). Voltage dependence of macroscopic and unitary currents of gap junction channels formed by mouse connexin50 expressed in rat neuroblastoma cells. *The Journal of Physiology*, *517*(Pt 3), 673–689. https://doi.org/10.1111/j.1469-7793.1999.0673s.x

Srinivas, M., Kronengold, J., Bukauskas, F. F., Bargiello, T. A., & Verselis, V. K. (2005). Correlative studies of gating in Cx46 and Cx50 hemichannels and gap junction channels. *Biophysical Journal*, *88*(3), 1725–1739. https://doi.org/10.1529/biophysj.104.054023

Tong, J.-J., & Ebihara, L. (2006). Structural Determinants for the Differences in Voltage Gating of Chicken Cx56 and Cx45.6 Gap-Junctional Hemichannels. *Biophysical Journal*, *91*(6), 2142–2154. https://doi.org/10.1529/biophysj.106.082859

Tong, J.-J., Khan, U., Haddad, B. G., Reichow, S. L., & Ebihara, L. (2021). *Gain-of-function in a cataract-associated mutation in connexin-50 by stabilization and neutralization of the voltage-sensing domain* [In preparation].

Tong, J.-J., Liu, X., Dong, L., & Ebihara, L. (2004). Exchange of Gating Properties Between Rat Cx46 and Chicken Cx45.6. *Biophysical Journal*, *87*(4), 2397–2406. https://doi.org/10.1529/BIOPHYSJ.104.039594

Tong, J.-J., Sohn, B. C. H., Lam, A., Walters, D. E., Vertel, B. M., & Ebihara, L. (2013). Properties of two cataract-associated mutations located in the NH2 terminus of connexin 46. *American Journal of Physiology - Cell Physiology*, *304*(9), C823–C832. https://doi.org/10.1152/ajpcell.00344.2012

Tong, X., Aoyama, H., Tsukihara, T., & Bai, D. (2014). Charge at the 46th residue of connexin 50 is crucial for the gap-junctional unitary conductance and transjunctional voltage-dependent gating. *The Journal of Physiology*, *592*(23), 5187–5202. https://doi.org/10.1113/jphysiol.2014.280636

Trexler, E. B., Bennett, M. V. L., Bargiello, T. A., & Verselis, V. K. (1996). Voltage gating and permeation in a gap junction hemichannel. *Proceedings of the National Academy of Sciences of the United States of America*, *93*(12), 5836–5841.

Veenstra, R. D. (2016). Establishment of the Dual Whole Cell Recording Patch Clamp Configuration for the Measurement of Gap Junction Conductance. *Methods in Molecular Biology (Clifton, N.J.)*, *1437*, 213–231. https://doi.org/10.1007/978-1-4939-3664-9_16

Verselis, V. K., Ginter, C. S., & Bargiello, T. A. (1994). Opposite voltage gating polarities of two closely related onnexins. *Nature*, *368*(6469), 348–351. https://doi.org/10.1038/368348a0

Wang, Z., & Schey, K. L. (2009). Phosphorylation and truncation sites of bovine lens connexin 46 and connexin 50. *Experimental Eye Research*, *89*(6), 898–904. https://doi.org/10.1016/j.exer.2009.07.015

Waterhouse, A., Bertoni, M., Bienert, S., Studer, G., Tauriello, G., Gumienny, R., Heer, F. T., de Beer, T. A. P., Rempfer, C., Bordoli, L., Lepore, R., & Schwede, T. (2018). SWISS-MODEL: Homology modelling of protein structures and complexes. *Nucleic Acids Research*, *46*(W1), W296–W303. https://doi.org/10.1093/nar/gky427

Wu, E. L., Cheng, X., Jo, S., Rui, H., Song, K. C., Dávila-Contreras, E. M., Qi, Y., Lee, J., Monje-Galvan, V., Venable, R. M., Klauda, J. B., & Im, W. (2014). CHARMM-GUI Membrane Builder toward realistic biological membrane simulations. *Journal of Computational Chemistry*, *35*(27), 1997–2004. https://doi.org/10.1002/jcc.23702

Xin, L., & Bai, D. (2013). Functional roles of the amino terminal domain in determining biophysical properties of Cx50 gap junction channels. *Frontiers in Physiology*, *4*. https://doi.org/10.3389/fphys.2013.00373

Xin, L., Gong, X.-Q., & Bai, D. (2010). The Role of Amino Terminus of Mouse Cx50 in Determining Transjunctional Voltage-Dependent Gating and Unitary Conductance. *Biophysical Journal*, *99*(7), 2077–2086. https://doi.org/10.1016/J.BPJ.2010.07.032

Xu, Q., Lin, X., Matiukas, A., Zhang, X., & Veenstra, R. D. (2016). Specificity of the connexin W3/4 locus for functional gap junction formation. *Channels (Austin, Tex.)*, *10*(6), 453–465. https://doi.org/10.1080/19336950.2016.1200775

Yue, B., Haddad, B. G., Khan, U., Chen, H., Atalla, M., Zhang, Z., Zuckerman, D. M., Reichow, S. L., & Bai, D. (2021). Connexin 46 and connexin 50 gap junction channel properties are shaped by structural and dynamic features of their N-terminal domains. *The Journal of Physiology*. https://doi.org/10.1113/JP281339